Electronic Supplementary Information

Cubic spline-based depth-dependent localization of mitochondria–endoplasmic reticulum contacts by three-dimensional light-sheet super-resolution microscopy

Yucheng Sun,[a1] Seungah Lee[b1] and Seong Ho Kang*[ab]

[a]*Department of Chemistry, Graduate School, Kyung Hee University, Yongin-si, Gyeonggi-do 17104, Republic of Korea*

[b]*Department of Applied Chemistry and Institute of Natural Sciences, Kyung Hee University, Yongin-si, Gyeonggi-do 17104, Republic of Korea*

---

*Corresponding authors:

Seong Ho Kang: Phone, +82-31-201-3349; e-mail, shkang@khu.ac.kr.

[1]These authors contributed equally to this work.

Contents

Movie M1. Depth-dependent localization of 5 nm AuNP, 12 nm AuNP, and 20 nm AgNP on a coverslip

Movie M2. Depth-dependent localization of 20 nm AuNP, 40 nm AgNP, and 80 nm AgNP on a coverslip

Movie M3. 3D super-resolution image of 12 nm AuNP and 20 nm AgNPs in a HeLa cell shown in Fig. 5g1

Movie M4. 3D super-resolution image of 12 nm AuNP and 20 nm AgNP in a HeLa cell shown in Fig. 5g2

Movie M5. 3D super-resolution image of 12 nm AuNP and 20 nm AgNP in a HeLa cell shown in Fig. 5g3

Movie M6. 3D super-resolution image of 12 nm AuNP and 20 nm AgNP in a HEK293 cell shown in Fig. 6e

Movie M7. 3D super-resolution image of 12 nm AuNP and 20 nm AgNP in a RAW264.7 macrophage cell shown in Fig. S11e

Movie M8. 3D super-resolution image of 12 nm AuNP and 20 nm AgNP in an AGS macrophage cell shown in Fig. S12e

Movie M9. 3D super-resolution image of 12 nm AuNP and 20 nm AgNP in an HT29 cell shown in Fig. S13e

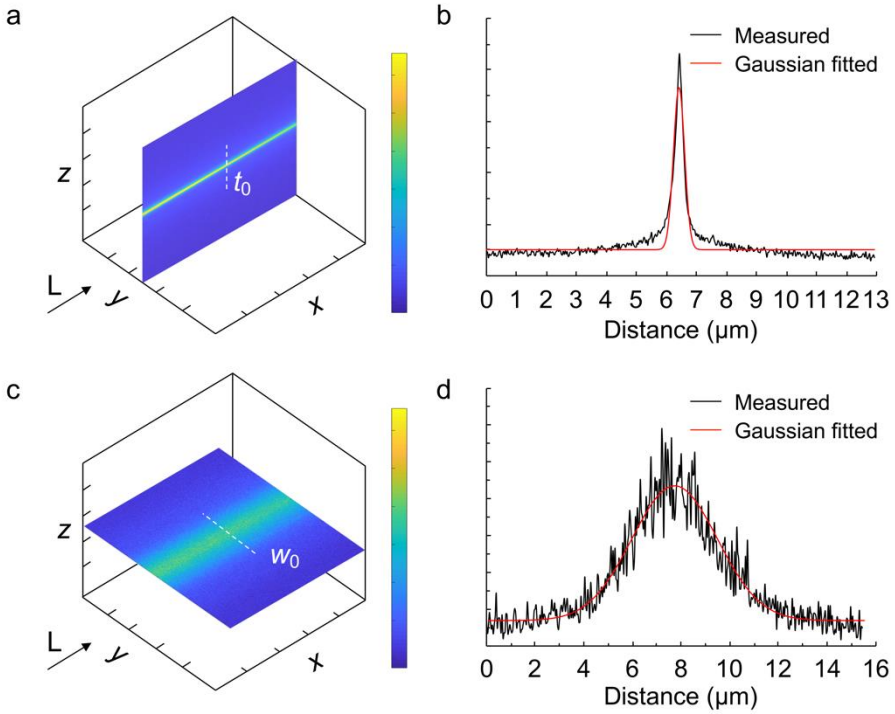

Fig. S1 Characterization of the light sheet beam by a 10× objective lens. (a) Side view of the beam. (b) Intensity plot of the white dotted line in (a). (c) Top view of the beam. (d) Intensity plot of the white dotted line in (c).

Experimental section: A concentrated fluorescent dye (rhodamine B) solution was filled into the flow chamber (i.e., cuvette for fluorescence). By adjusting the illumination objective lens, the light sheet was pass through the fluorescent solution to form a bright line exhibiting top view images. The side view of beam was imaged under the condition of spatially rotating cylindrical lens in *xz* plane with 90 degrees resulting in the spinning of light sheet beam. This light sheet was imaged by the detecting objective lens and recorded by the EMCCD camera.

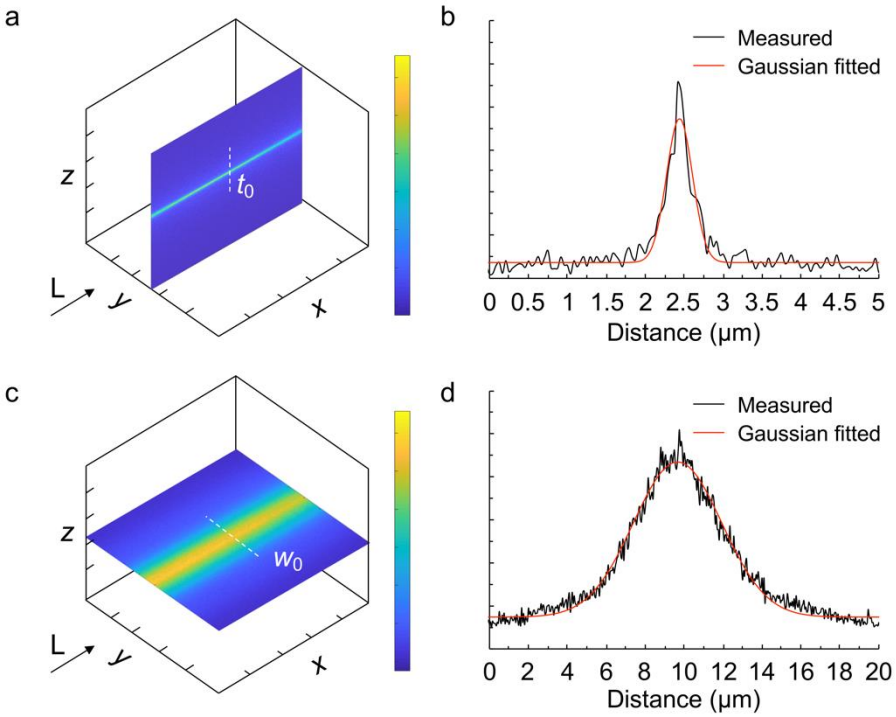

Fig. S2 Characterization of the light sheet beam by a 20× objective lens. (a) Side view of the beam. (b) Intensity plot of the white dotted line in (a). (c) Top view of the beam. (d) Intensity plot of the white dotted line in (c).

Experimental section: A concentrated fluorescent dye (rhodamine B) solution was filled into the flow chamber (i.e., cuvette for fluorescence). By adjusting the illumination objective lens, the light sheet was pass through the fluorescent solution to form a bright line exhibiting top view images. The side view of beam was imaged under the condition of spatially rotating cylindrical lens in *xz* plane with 90 degrees resulting in the spinning of light sheet beam. This light sheet was imaged by the detecting objective lens and recorded by the EMCCD camera.

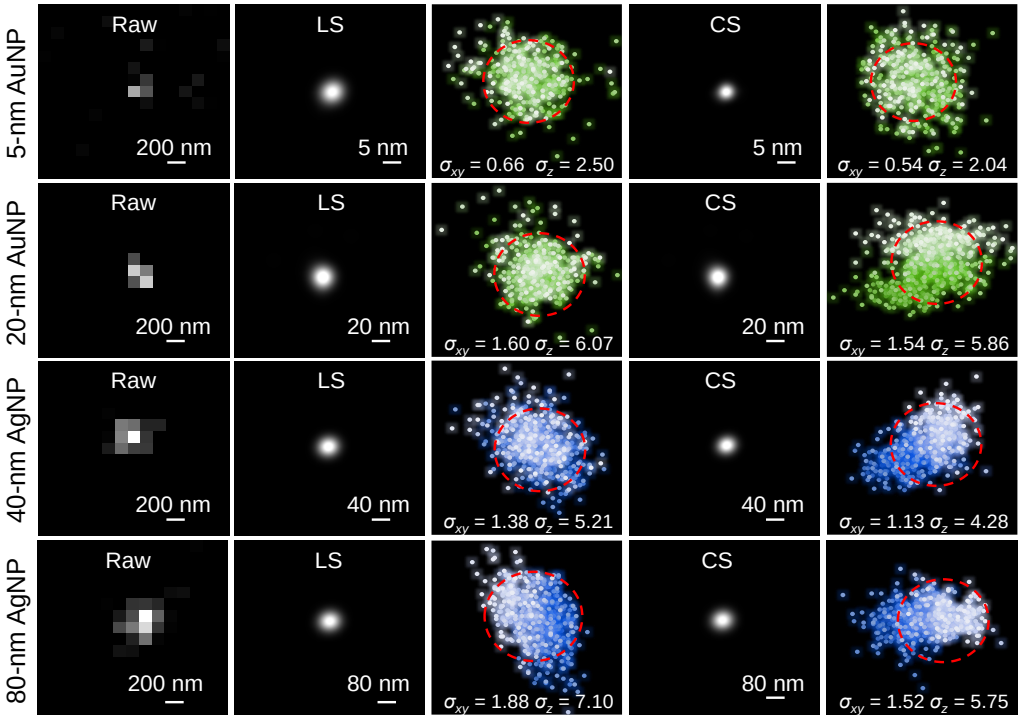

Fig. S3 Comparison of the localization precision of NPs by least squares and cubic spline algorithms. Each NP was imaged at the $z = 0$ position with 500 frames and z sliced in 10 nm steps with 1000 frames. Lateral precision (σ_{xy}) was obtained by two localization algorithms, and axial precision (σ_z) was calculated from σ_{xy} using the Born–Wolf model.

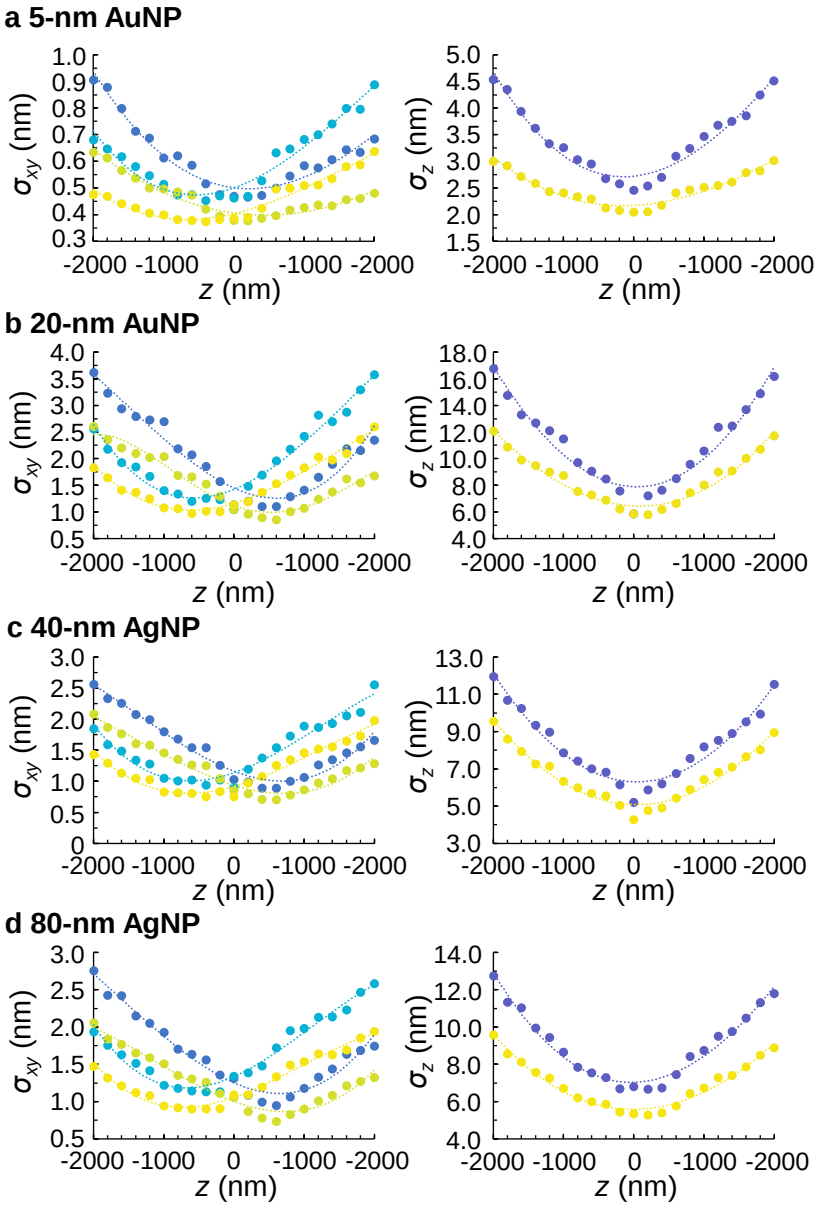

Fig. S4 Comparison of localization precision on different axial positions by two localization methods. (a) 5 nm AuNP. (b) 20 nm AuNP. (c) 40 nm AgNP. (d) 80 nm AgNP. Tufts blue, turquoise green, and iris purple dots represent localization by method A. Pear yellow, apple yellow, and dandelion yellow dots represent localization by method B.

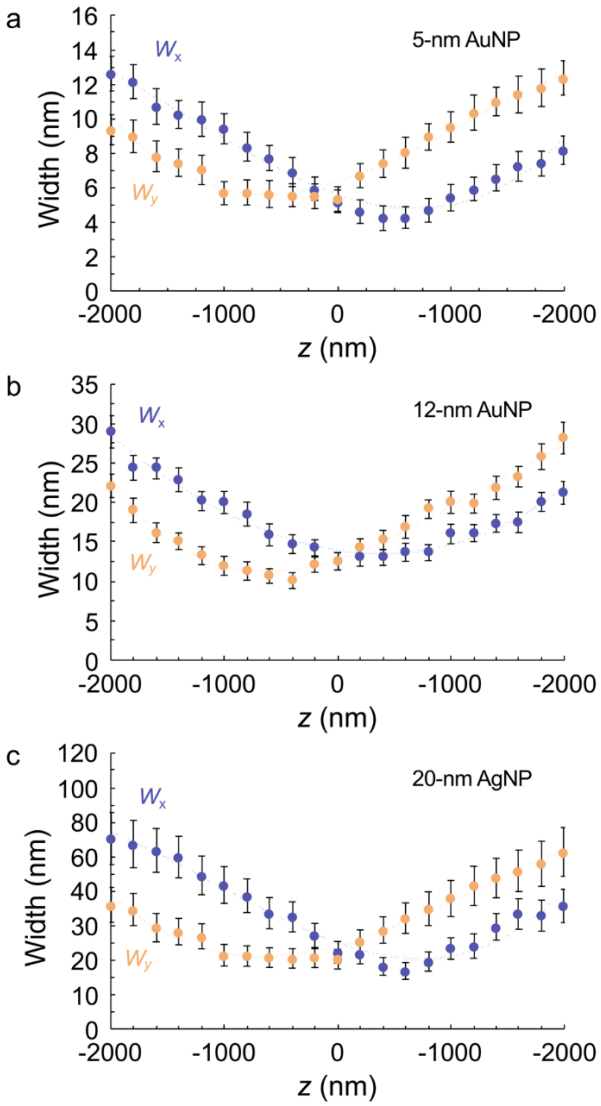

Fig. S5 Calibration curves of PSF widths from NPs at various axial positions. (a) 5 nm AuNP. (b) 12 nm AuNP. (c) 20 nm AgNP.

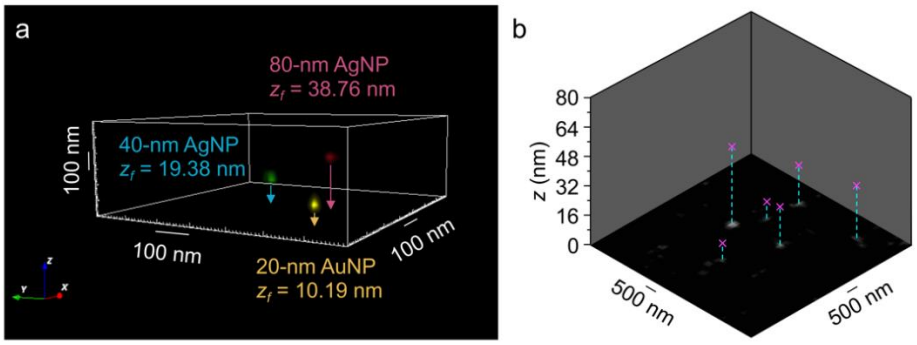

Fig. S6 Depth-dependent localization of NPs. (a) Reconstructed image of the depth-dependent localization of 20 nm AuNP, 40 nm AgNP, and 80 nm AgNP on a PLL-coated coverslip. (b) Wide-field raw image of the depth-dependent localization of mixed 20 nm AuNP, 40 nm AgNP, and 80 nm AgNP on a PLL-coated coverslip. Purple markers represented the height of focused plane on NPs.

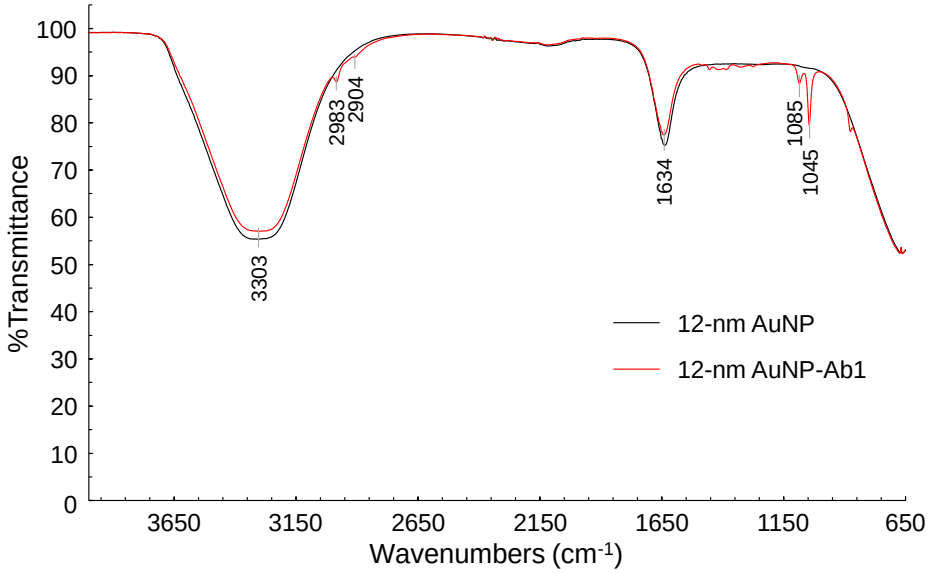

Fig. S7 FT-IR spectrum of 12 nm AuNP and 12 nm AuNP-Ab1. The spectrum was obtained in the range of 650–4000 cm^{-1} with a Nicolet iN 10 MX FT-IR imaging microscope from Thermo Fisher Scientific (Waltham, MA). AuNP-Ab1: AuNPs conjugated with antibodies targeted to mitochondria.

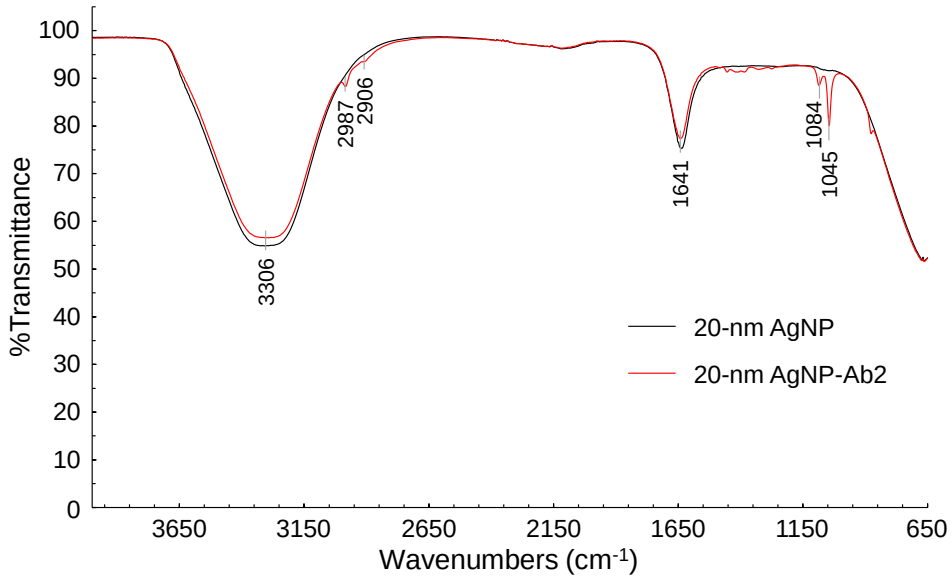

Fig. S8 FT-IR spectrum of 20 nm AgNP and 20 nm AgNP-Ab2. The spectrum was obtained in the range of 650–4000 cm^{-1} with a Nicolet iN 10 MX FT-IR imaging microscope from Thermo Fisher Scientific (Waltham, MA). AgNP-Ab2: AgNPs conjugated with antibodies targeted to ER.

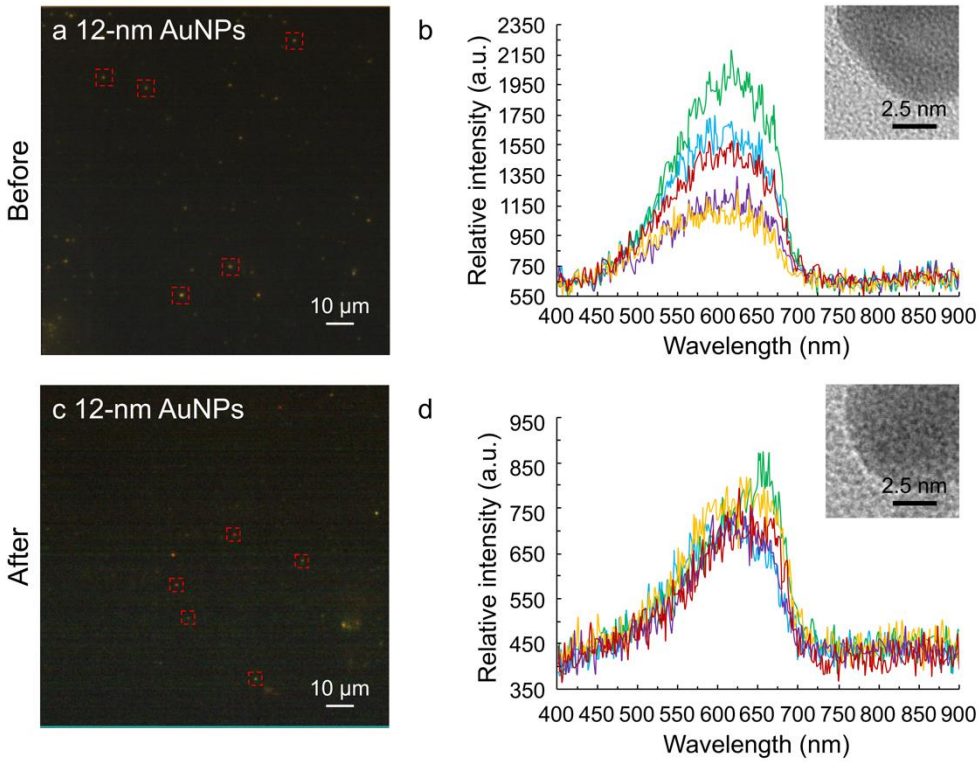

Fig. S9 Hyperspectral and TEM images of 12 nm AuNPs before and after conjugation. (a) Hyperspectral images of bare 12 nm AuNPs. (b) Resonant scattering peaks generated from (a). (c) Hyperspectral images of 12 nm AuNPs-conjugated with antibodies. (d) Resonant scattering peaks generated from (c). Insets in (b) and (d) are the TEM images of 12 nm AuNPs before and after conjugation of antibodies, respectively.

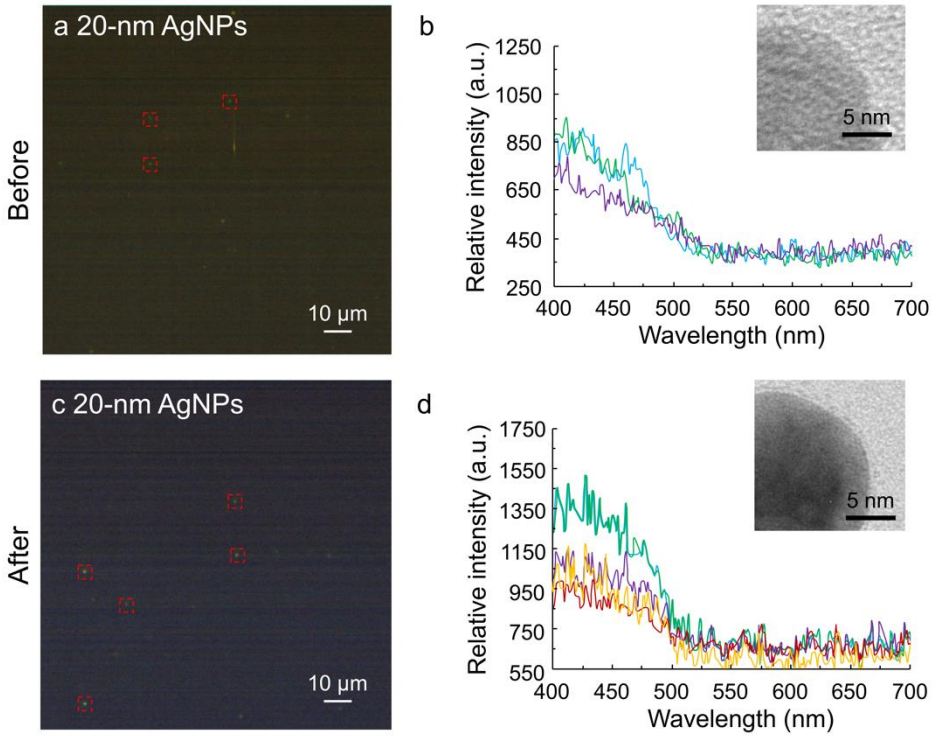

Fig. S10 Hyperspectral and TEM images of 20 nm AgNPs before and after conjugation. (a) Hyperspectral images of bare 20 nm AgNPs. (b) Resonant scattering peaks generated from (a). (c) Hyperspectral images of 20 nm AgNPs conjugated with antibodies. (d) Resonant scattering peaks generated from (c). Insets in (b) and (d) are the TEM images of 20 nm AgNPs before and after the conjugation of antibodies, respectively.

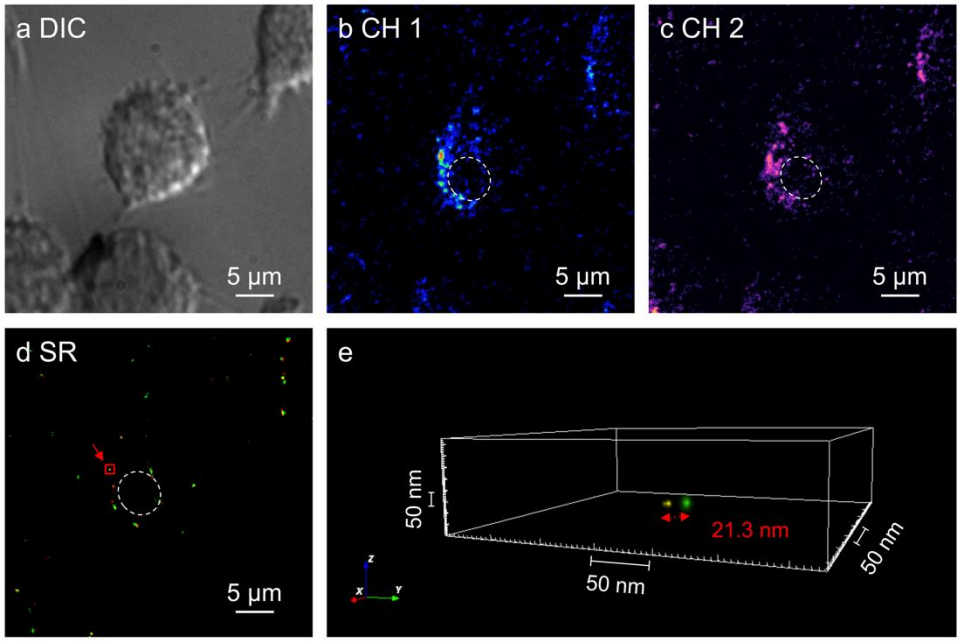

Fig. S11 Images of Mito–12 nm AuNPs and ER–20 nm AgNPs in RAW264.7 cells obtained by DIC microscopy and 3D LSRM. (a) DIC image of the RAW264.7 macrophage cell. (b) and (c) Raw scattering images of 12 nm AuNPs and 20 nm AgNPs in a cell, respectively. (d) 2D reconstructed image of nanoparticles in cells. (e) 3D super-resolution image of adjacent 12 nm AuNP and 20 nm AgNPs shown in (d). CH1: 520/15 nm bandpass filter. CH2: 406/13 nm bandpass filter.

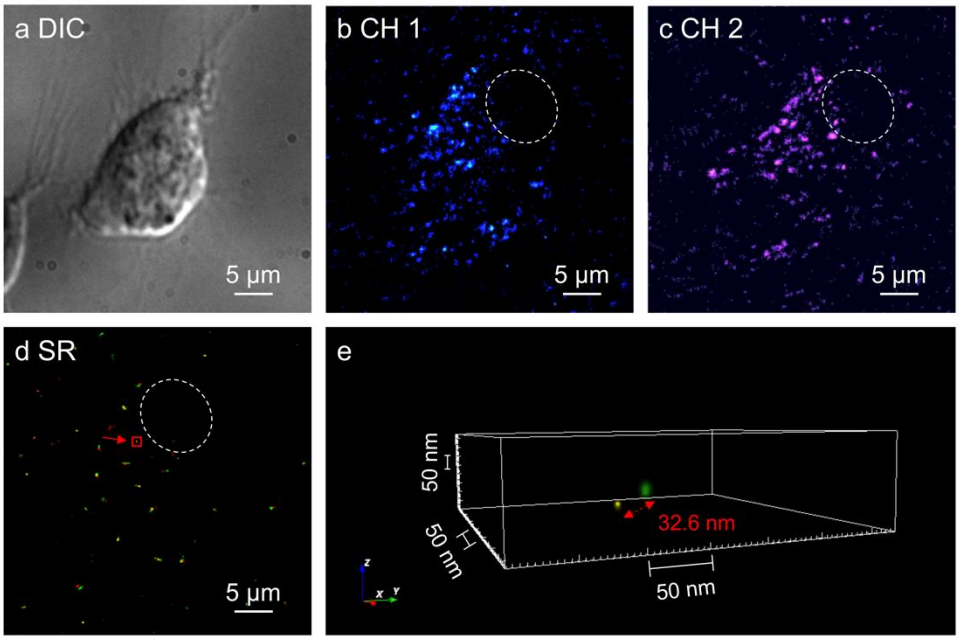

Fig. S12 Images of Mito–12 nm AuNPs and ER–20 nm AgNPs in AGS cells obtained by DIC microscopy and 3D LSRM. (a) DIC image of an AGS cell. (b) and (c) Raw scattering images of 12 nm AuNPs and 20 nm AgNPs in a cell, respectively. (d) 2D reconstructed image of nanoparticles in cells. (e) 3D super-resolution image of adjacent 12 nm AuNP and 20 nm AgNPs shown in (d). CH1: 520/15 nm bandpass filter. CH2: 406/13 nm bandpass filter.

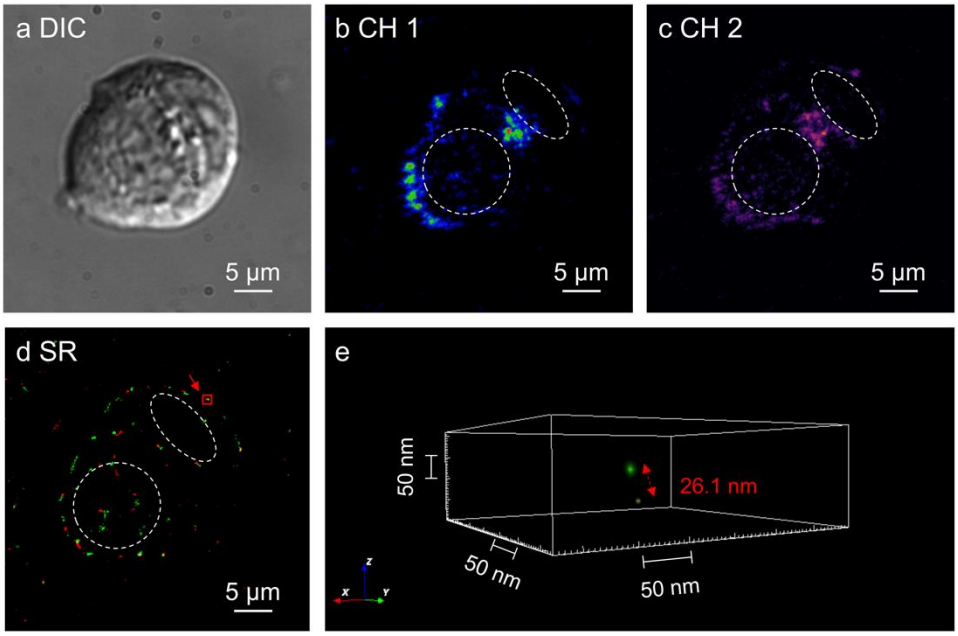

Fig. S13 Images of Mito–12 nm AuNPs and ER–20 nm AgNPs in HT29 cells obtained by DIC microscopy and 3D LSRM. (a) DIC image of an HT29 cell. (b) and (c) Raw scattering images of Mito–12 nm AuNPs and ER–20 nm AgNPs in a cell, respectively. (d) 2D reconstructed image of nanoparticles in cells. (e) 3D super-resolution image of adjacent 12 nm AuNP and 20 nm AgNPs shown in (d). CH1: 520/15 nm bandpass filter. CH2: 406/13 nm bandpass filter.

Table S1 Distances between Mito and ER in HeLa cells calculated by cubic spline algorithm-based depth-dependent fluorescence-free 3D LSRM

HeLa Cell	Contacts	Distance (nm)	Mean (±SD) (nm)
	1	18.7	
1	2	20.4	20.8 (±2.3)
	3	23.3	
	1	20.6	
2	2	19.7	19.4 (±1.4)
	3	17.8	
	1	20.2	
3	2	21.5	25.4 (±7.9)
	3	34.5	
	1	23.7	
4	2	18.8	20.0 (±3.3)
	3	17.4	
	1	23.9	
5	2	28.3	26.2 (±2.2)
	3	26.5	
	1	21.1	
6	2	18.4	21.1 (±2.8)
	3	23.9	
	1	27.6	
7	2	25.4	23.8 (±4.9)
	3	18.3	

Table S2 Distances between Mito and ER in RAW264.7 macrophage and AGS cells calculated by cubic spline algorithm-based depth-dependent fluorescence-free 3D LSRM

Cell		Contacts	Distance (nm)	Mean (±SD) (nm)
RAW264.7 macrophage	1	1	21.3	21.4 (±4.3)
		2	17.2	
		3	25.8	
	2	1	16.9	23.2 (±8.1)
		2	32.3	
		3	20.4	
	3	1	22.7	22.0 (±2.9)
		2	18.8	
		3	24.4	
AGS human gastric cancer	1	1	32.6	24.4 (±7.1)
		2	21.1	
		3	19.5	
	2	1	17.7	19.6 (±3.0)
		2	23.1	
		3	18.0	
	3	1	19.6	21.8 (±4.9)
		2	27.4	
		3	18.3	

Table S3 Distances between Mito and ER in HT29 and HEK293 cells calculated by cubic spline algorithm-based depth-dependent fluorescence-free 3D LSRM

Cell		Contacts	Distance (nm)	Mean (±SD) (nm)
HT29	1	1	26.1	22.2 (±3.8)
		2	18.5	
		3	21.9	
	2	1	25.3	23.2 (±4.6)
		2	17.9	
		3	26.3	
	3	1	18.0	18.8 (±0.8)
		2	19.6	
		3	18.7	
HEK293	1	1	26.1	25.2 (±2.1)
		2	24.4	
		3	27.6	
	2	1	23.7	19.3 (±1.9)
		2	17.6	
		3	21.3	
	3	1	18.9	19.3 (±0.8)
		2	18.5	
		3	20.1	